Energy Engineering

Tech Science Press

https://doi.org/10.32604/ee.2026.083105

ARTICLE

Molecular Dynamics Study of the Wetting Behavior of Biodiesel Combustion Particles under Exhaust-Plume Conditions

Yifan Liu[1], Dengpan Zhang[1,*], Jiayi Du[1], Deqing Mei[1] and Yinnan Yuan[2]

[1]School of Automotive and Traffic Engineering, Jiangsu University, Zhenjiang, China
[2]College of Energy, Soochow University, Suzhou, China

*Corresponding Author: Dengpan Zhang. Email: zhdp@ujs.edu.cn

Received: 29 March 2026; Accepted: 18 May 2026; Published: 18 June 2026

ABSTRACT: The hygroscopic growth of engine-emitted particulate matter in exhaust plumes is strongly influenced by surface wettability. In this study, molecular dynamics simulations were performed on biodiesel- and diesel-derived combustion-particle models constructed on a unified defective carbon framework to investigate wetting behavior under representative exhaust-plume temperature and humidity conditions. Under the reference condition of 333 K and a saturation ratio of 1.2, the equilibrium contact angles on smooth biodiesel, rough biodiesel, and rough diesel surfaces were 45.4°, 63.5°, and 95.5°, respectively. The trends in work of adhesion and interfacial hydrogen-bond statistics were consistent with the contact-angle results. Temperature primarily modulates interfacial water exchange and liquid-phase rearrangement, whereas the saturation ratio affects the availability of vapor-phase water and its contribution to rearrangement near the contact line and stable solid-liquid bonding. Ultimately, particle wetting behavior is governed by the competition among four interdependent processes: vapor-phase water supply, liquid-phase rearrangement, interfacial bonding, and contact-line motion. Radial distribution function (RDF) analysis, interfacial hydrogen-bond statistics, and spatially resolved profiles of interfacial density and local pressure show that, relative to diesel combustion particles, biodiesel combustion particles—with a higher density of surface oxygen functionalities—exhibit stronger interfacial water enrichment, a denser hydration layer, and more stable interfacial bonding. These differences are consistent with their smaller equilibrium contact angle and greater wetting propensity. These results provide molecular-scale insight into particle-water interactions relevant to early hygroscopic growth in exhaust-plume environments.

KEYWORDS: Biodiesel; particulate matter; wetting behavior; molecular dynamics; exhaust plume

1 Introduction

Engine-emitted particles are a major source of atmospheric ultrafine particles, and long-term exposure to polluted air substantially increases the risk of respiratory and cardiovascular disease [1]. When hot exhaust is discharged into the atmosphere, a plume region forms near the tailpipe. As particles disperse within this region, they undergo rapid dilution, cooling, and component redistribution. These processes markedly alter the local thermodynamic conditions and create favorable conditions for droplet formation and hygroscopic particle growth. Roadside measurements by Vogt et al. [2] showed that motor-vehicle exhaust experiences rapid dilution and cooling in the tailpipe plume, a process that is highly heterogeneous in both space and time. Under such conditions, the local microenvironment may pass through subsaturated, saturated, and supersaturated states, thereby promoting water-vapor condensation and subsequent hygroscopic growth through collisions and coagulation with combustion particles. Lipsky and Robinson [3] further showed that, once exhaust leaves the tailpipe, both particle mass and the partitioning of semivolatile species change rapidly during dilution. The surface chemical composition of carbonaceous particles and their mixing state with other components strongly influence hygroscopicity [4–6]. The binary homogeneous nucleation model developed by Vehkamäki et al. [7] indicates that typical temperatures in the engine-exhaust plume region range from 300 to 400 K. The initial wetting process between particles and water droplets not only determines the initial state of particles during atmospheric dispersion but also affects particle-size evolution, residence time, and the radiative effects of atmospheric aerosols [8].

Field and bench-scale experiments are limited by temporal resolution and spatial scale, making it difficult to resolve the molecular-scale mechanisms underlying wettability evolution. Molecular dynamics simulations, however, provide an effective means of probing the wettability of carbonaceous surfaces. Taherian et al. [9] showed that graphene-based models can adequately describe wetting at carbon-water interfaces. Werder et al. [10] further proposed a widely used parameter set for carbon-water interactions. Building on these foundational studies, subsequent investigations into the interfacial structure of liquids, thermodynamically consistent definitions of contact angle, and nanoscale wetting dynamics have significantly deepened our mechanistic understanding of carbon–water interfaces [11,12]. Additional studies have shown that contact-line pinning, contact-angle hysteresis, and pinning-depinning processes on rough or chemically heterogeneous surfaces can strongly influence the apparent wetting behavior of nanodroplets [13–16]. Molecular dynamics simulations of wetting on combustion-particle surfaces can therefore help elucidate the microscopic mechanisms governing hygroscopic particle growth from the perspective of interfacial structure and molecular exchange.

As a renewable, carbon-neutral fuel, biodiesel offers an important route for reducing carbon emissions from diesel engines. Compared with fossil diesel, biodiesel-derived combustion particles generally contain a higher fraction of oxygen-containing surface sites, including hydroxyl, carbonyl, and carboxyl groups [17–19]. These particles can undergo pronounced condensational growth during cooling and dilution [20], and their hygroscopicity is closely related to their surface chemical state [4,21]. Surface oxygen-containing functional groups on biodiesel combustion particles are generally associated with greater hydrophilicity [22,23]. However, despite extensive molecular dynamics studies of wetting on model carbonaceous surfaces, including graphene, carbon black, and idealized graphite, the molecular mechanisms by which surface oxygen functionalities and nanoscale roughness jointly regulate wetting behavior under representative plume-region temperature and humidity conditions remain insufficiently understood.

In this study, representative functional groups of combustion particles were introduced onto a unified defective carbon framework to construct biodiesel and diesel combustion-particle models. Molecular dynamics simulations were then performed to investigate the wetting behavior of these particles under representative plume-region temperature and humidity conditions. By analyzing the equilibrium contact angle, work of adhesion, and competitive interfacial processes, this study elucidates the microscopic mechanisms governing wetting between combustion particles and water droplets and provides a basis for understanding the secondary growth and evolution of biodiesel combustion particles in the atmosphere.

2 Model Construction and Methodology

2.1 Development of Simulation Model

Biodiesel and diesel combustion particles differ markedly in the distribution of oxygen-containing surface sites. XPS results reported in Ref. [19] showed that, relative to diesel combustion particles, the surface O/C ratio of particles emitted from soybean-, palm-, and waste-cooking-oil biodiesel increased by 40.4%, 45.1%, and 48.9%, respectively. The relative abundance of hydroxyl (-OH) increased from 2.1% to 3.2%, 5.4%, and 6.8%, respectively, whereas that of carbonyl (C=O) increased from 0.7% to 0.9%–1.3%. Combined with nanoparticle structural characterization results [24], these data were used to select and parameterize representative functional groups on the unified defective carbon framework. Since the O/C ratio obtained from X-ray photoelectron spectroscopy (XPS) represents an integrated surface signal, directly equating it with the grafted oxygen content in the computational model would systematically overestimate interfacial polarity and wettability. To ensure physical realism and model robustness, a conservative effective O/C ratio was employed as a structural constraint. Functional-group fractions were normalized to the number of graftable carbon sites on the surface, and grafting densities were reported per 100 surface carbon atoms. For particles derived from biodiesel combustion, the effective O/C ratio was assigned a value of 0.20. The relative site fractions of hydroxyl and carbonyl groups were set to 4% and 1%, respectively. The remaining oxygen content under the O/C-ratio constraint was assigned to carboxyl (-COOH), methoxy (-OCH3), and methyl ester (-COOCH3) groups. For diesel combustion particles, the O/C ratio was set to 0.09. The relative site fractions of hydroxyl and carbonyl groups were set to 2% and 1%, respectively. The remaining oxygen content under the O/C-ratio constraint was assigned to C-O-C and anhydride (-CO-O-CO-) groups.

Fig. 1 shows the three surface models constructed in this study: a graphene framework containing vacancies and Stone-Wales defects, a functionalized biodiesel combustion-particle surface, and a functionalized diesel combustion-particle surface. The graphene framework provides a unified topological reference, whereas the two functionalized surfaces capture the chemical distinctions between particles derived from different fuels. A rough spherical particle with a diameter of 14 nm was constructed by grafting the corresponding functional groups onto defective graphene. To isolate the effect of surface morphology, a smooth biodiesel combustion particle was additionally constructed as a control surface with the same functional-group composition as the rough biodiesel model.

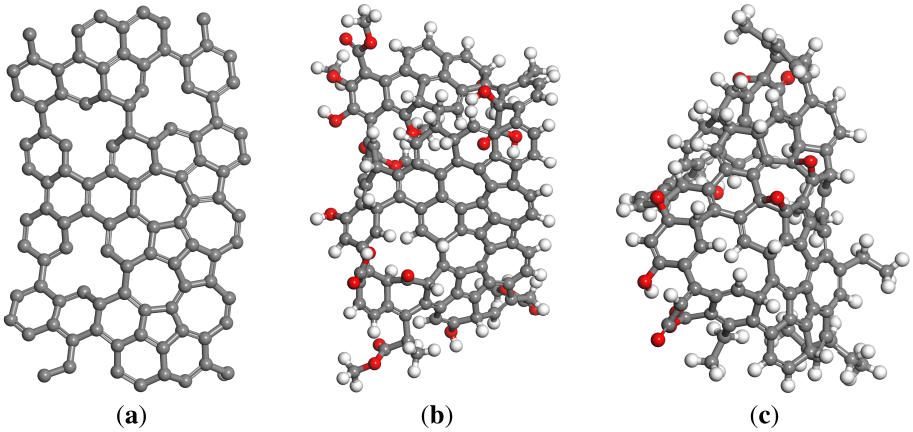

Figure 1: Defective framework and functionalized particle-surface models. (**a**) Graphene framework; (**b**) biodiesel combustion particle framework; (**c**) diesel combustion particle framework.

Molecular dynamics simulations were performed to investigate the wetting behavior of water droplets on particle surfaces. Nonbonded interactions in the system comprised electrostatic and van der Waals contributions. Electrostatic interactions were represented by Coulombic interactions between atomic point charges. Nonbonded interactions within the solid phase, including those between the carbon framework and oxygen-containing functional groups, were described using the PCFF-like Class II force field [25]. The van der Waals interaction energy was calculated as:

$$E_{vdW} = \varepsilon\left[2\left(\frac{\delta_0}{r}\right)^9 - 3\left(\frac{\delta_0}{r}\right)^6\right] \tag{1}$$

where ε denotes the potential-well depth, δ_0 denotes the equilibrium separation corresponding to the minimum potential energy, and r denotes the interparticle distance.

The water phase was modeled with SPC/E [26], and molecular geometry was constrained using SHAKE. Cross-phase van der Waals parameters for solid-liquid interactions were obtained from the atomic characteristic lengths and potential-well depths using the Lorentz-Berthelot mixing rules:

$$\sigma_{ij} = \frac{\sigma_i + \sigma_j}{2}, \varepsilon_{ij} = \left(\varepsilon_i \varepsilon_j\right)^{\frac{1}{2}} \tag{2}$$

where σ_{ij} and ε_{ij} denote the mixed characteristic length and potential-well depth between atoms i and j, respectively, and σ_i, σ_j, ε_i, and ε_j are the corresponding force-field parameters for atoms i and j.

Simulations were carried out in LAMMPS using real units and three-dimensional periodic boundary conditions. The simulation box measured 25.0 nm × 25.0 nm × 30.0 nm, the water droplet diameter was 6 nm, and the nonbonded cutoff radius was 12.0 Å. Initially, the water droplet was separated from the particle surface by approximately 8.5 Å. Detailed model parameters are listed in Table 1. The saturation ratio was prescribed by adjusting the number of gas-phase water molecules and was defined as:

$$S = \frac{p_v}{p_{sat}(T)} \tag{3}$$

where p_v is the water-vapor partial pressure calculated from the initial number of gas-phase water molecules and the available gas-phase volume, and $p_{sat}(T)$ is the saturation vapor pressure of water at the target temperature T.

Table 1: Model parameters.

Parameter Category	Parameter	Value	Source
System	Simulation box size	25.0 × 25.0 × 30.0 nm^3	
	Number of water molecules in droplet	3794	
	Initial particle diameter	14 nm	
	Effective O/C ratio	0.20/0.09	[19]
Force field	Solid phase/water model	PCFF/SPC/E	[25,26]
	LJ scaling factor	0.65	[10]
Numerical setting	Time step	2.0 fs	
	Cutoff/long-range electrostatics	12.0 Å; PPPM (10^{-4})	
Procedure	Annealing/equilibration/production	2.2/10.0/1.0 ns	
	Total simulation time	13.2 ns	

Here, S characterizes the initial humidity condition corresponding to the prescribed gas-phase water content. Because the simulations were performed in a closed system with periodic boundary conditions, S should be interpreted as an initial thermodynamic descriptor rather than as an instantaneous saturation ratio maintained throughout the trajectory. To reduce periodic-image effects on droplet-particle interactions, a gas-phase buffer was retained between the droplet-particle system and the simulation boundaries, and long-range electrostatic interactions were treated using the particle-particle particle-mesh (PPPM) method.

The simulation procedure comprised four steps: (1) conjugate-gradient minimization; (2) 2.2 ns of cyclic annealing over 300 K → 420 K → 300 K; (3) extended equilibration at the target temperature; and (4) production sampling over the late-stage plateau region. Unless otherwise specified, each system was equilibrated for 10.0 ns and sampled for 1.0 ns, giving a total simulation time of 13.2 ns. The contact angle, work of adhesion, and interfacial statistics were obtained from the late-stage plateau region. Cyclic annealing was used to reduce dependence on the initial configuration and to help the contact line cross local metastable states on rough surfaces under controlled thermal perturbation, consistent with the thermally activated nature of contact-line motion on nanoscale rough surfaces [15,16]. Before production sampling, the contact angle, droplet center of mass, primary droplet-cluster size, and solid-liquid interaction energy were monitored to confirm that no systematic drift remained.

To evaluate the stability of the interfacial hydrogen-bond network, interfacial hydrogen bonds were identified using a donor-oxygen-to-acceptor-oxygen distance of less than 3.5 Å and an angle greater than 120° between the donor O-H bond and the acceptor oxygen atom. They were classified according to donor identity as water-donor and surface-donor hydrogen bonds. In water-donor hydrogen bonds, water molecules act as donors and surface oxygen sites act as acceptors; in surface-donor hydrogen bonds, surface hydroxyl or carboxyl groups act as donors and water oxygen atoms act as acceptors. The two types were counted separately, and the continuous hydrogen-bond autocorrelation function $C_{HB}(t)$ was used to characterize hydrogen-bond persistence:

$$C_{HB}(t) = \frac{\langle h_i(0)\, h_i(t)\rangle}{\langle h_i(0)\rangle} \tag{4}$$

where $h_i(t)$ is the continuous existence function of the ith initially identified interfacial hydrogen bond. For a bond identified at the initial time, $h_i(t)$ is assigned a value of 1 if the bond continuously satisfies the above geometric criteria over the interval from 0 to t, and 0 once the bond is interrupted. Angle brackets denote averaging over all initial times and the corresponding initial hydrogen bonds; the denominator normalizes $C_{HB}(0)$ to 1. The interfacial hydrogen-bond lifetime τ_{HB} is defined as the time at which $C_{HB}(t)$ decays to 1/e, namely $C_{HB}(\tau_{HB}) = 1/e$.

To investigate the wetting behavior of water droplets on particles under representative plume-region temperatures and saturation ratios, the simulation cases listed in Table 2 were designed. Saturation ratios of 0.8, 1.0, and 1.2 correspond to subsaturated, saturated, and supersaturated conditions, respectively. A temperature of 333 K represents an intermediate thermodynamic state during plume cooling and dilution, whereas a saturation ratio of 1.2 represents a potentially supersaturated state that may arise during strong mixing between hot exhaust and cold air. In the analysis, the condition of 333 K and a saturation ratio of 1.2 was defined as the reference case (Case 1).

Table 2: Simulation cases.

Case	Particle Type	Surface Feature	T (K)	Saturation Ratio	Effective O/C Ratio
Case 1	Biodiesel	Rough	333	1.2	0.20
Case 2	Biodiesel	Rough	300	1.2	0.20
Case 3	Biodiesel	Rough	360	1.2	0.20
Case 4	Biodiesel	Rough	333	1.0	0.20
Case 5	Biodiesel	Rough	300	1.0	0.20
Case 6	Biodiesel	Rough	360	1.0	0.20
Case 7	Biodiesel	Rough	333	0.8	0.20
Case 8	Biodiesel	Rough	300	0.8	0.20
Case 9	Biodiesel	Rough	360	0.8	0.20
Case 10	Biodiesel	Smooth	333	1.2	0.20
Case 11	Diesel	Rough	333	1.2	0.09

2.2 Model Validation

2.2.1 Repeatability of Contact-Angle Measurements

The equilibrium contact angle θ_{eq} was determined using a density-field-based central-slice method and used as the measure of apparent wettability; a smaller θ_{eq} indicates stronger wettability. Because the substrate was spherical, θ_{eq} was defined at the three-phase contact line as the angle between the tangent to the liquid-vapor interface and the local tangent to the particle surface [13,27–29], as shown in Fig. 2a. The water-density field was first averaged over a 200 ps moving window to reduce instantaneous thermal fluctuations during interface identification. The liquid-vapor interface was then extracted from the averaged density field in the central slice after excluding the near-wall first adsorbed water layer. Finally, the interface was extrapolated to the equivalent spherical solid surface, and θ_{eq} was obtained from the angle between the liquid-vapor and solid-surface tangents at the extrapolated intersection.

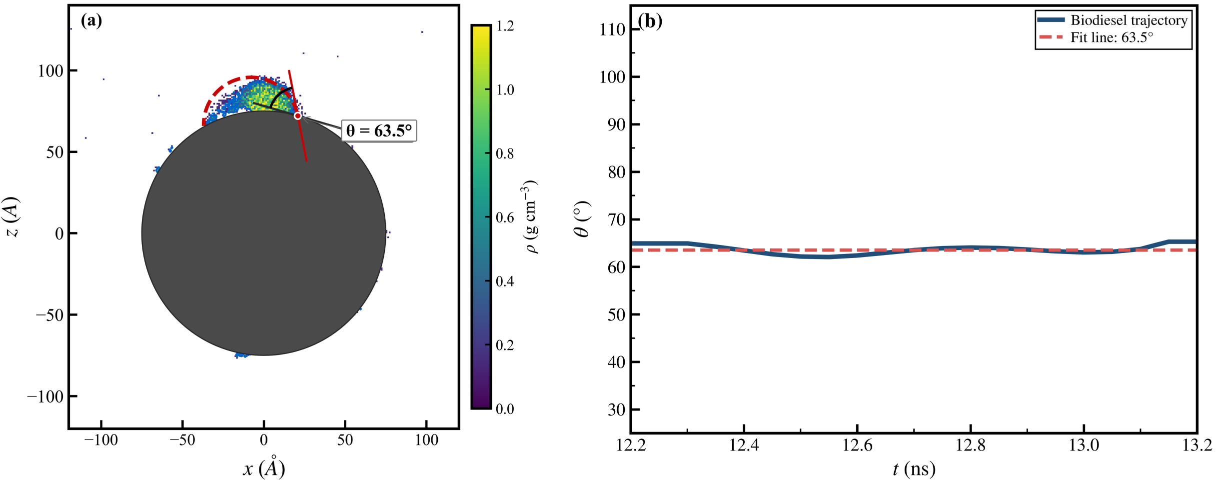

Figure 2: Schematic illustration of contact-angle extraction and time evolution in case 1.

The stability and uncertainty of the contact-angle statistics were evaluated using SEM(θ_{eq}) and $|\Delta\theta_{\mathrm{half}}|$. SEM($\theta_{\mathrm{eq}}$) denotes the standard error of the block-averaged contact angle obtained with a block size of 50 ps, and $|\Delta\theta_{\mathrm{half}}|$ denotes the absolute difference between the mean contact angles in the first and second halves of the sampling window. In Fig. 2b, SEM(θ_{eq}) is 0.26° and $|\Delta\theta_{\mathrm{half}}|$ is 0.79°, indicating that the contact angle remained statistically stable within the selected sampling window.

To assess repeatability, Case 1 was simulated independently three times, and the resulting equilibrium contact angles are compared in Fig. 3. The three simulations yielded equilibrium contact angles of 63.51°, 65.33°, and 64.73°, with a maximum deviation of 1.82°, indicating good repeatability.

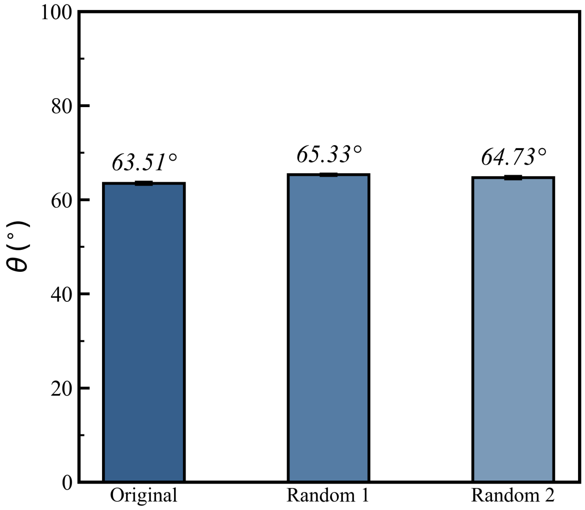

Figure 3: Repeatability of the contact angle in case 1.

2.2.2 Verification of Liquid-Vapor Interfacial Tension

To assess the suitability of the water model and the interfacial-tension calculation protocol, the liquid-vapor interfacial tension γ_{LV} was used as an independent calibration metric. The calculation setup is shown in Fig. 4, and the corresponding equation is:

$$\gamma_{LV} = \frac{L_z}{2}\left(P_{zz} - \frac{P_{xx} + P_{yy}}{2}\right) \tag{5}$$

where L_z is the length of the simulation box in the z direction, and P_{xx}, P_{yy}, and P_{zz} are the diagonal components of the pressure tensor. The pressure tensor was defined in the Irving-Kirkwood form [30], and the factor of 1/2 was used to account for the two liquid-vapor interfaces that coexist under periodic boundary conditions.

At 333 K, the calculated liquid-vapor interfacial tension γ_{LV} of the SPC/E water model is 53.1 mN·m^{-1}. This value is in close agreement with the 54.1 mN·m^{-1} reported in Ref. [31], with a relative deviation of about 1.8%. This agreement indicates that the water model and calculation procedure used in this study can reasonably represent liquid-vapor interfacial properties.

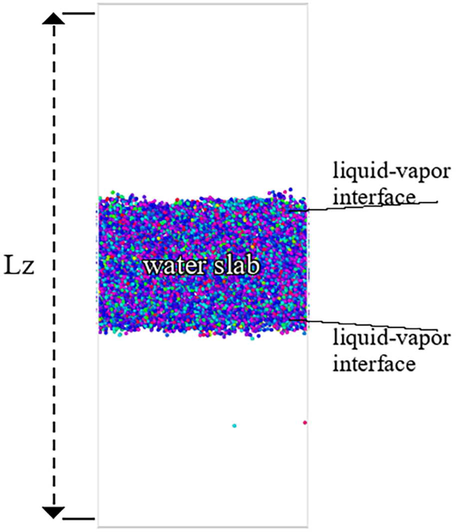

Figure 4: Schematic of the water-film method used to calculate liquid-vapor interfacial tension.

3 Results and Discussion

3.1 Wettability of Combustion Particles

Table 3 summarizes the equilibrium contact-angle statistics for water droplets on particle surfaces in all cases. SEM (θ_{eq}) ranges from 0.20° to 0.59°, and $|\Delta\theta_{half}|$ ranges from 0.14° to 1.46°, indicating that no sustained drift occurred during production sampling and that the resulting equilibrium contact angles can be used for wettability analysis.

Table 3: Contact-angle statistics during the production stage for all cases.

Case	θ_{eq} (°)	SEM (θ_{eq}) (°)	$\lvert\Delta\theta_{half}\rvert$ (°)
Case 1	63.51	0.26	0.79
Case 2	64.36	0.25	0.72
Case 3	59.15	0.41	1.24
Case 4	45.20	0.45	1.39
Case 5	51.83	0.25	0.95
Case 6	63.11	0.43	1.05
Case 7	38.90	0.20	0.38
Case 8	41.47	0.20	1.02
Case 9	62.38	0.54	0.32
Case 10	45.44	0.39	1.46
Case 11	95.47	0.59	0.14

At 333 K and a saturation ratio of 1.2, the variation of the equilibrium contact angle between water droplets and particle is shown in Fig. 5. As can be seen from the figure, the equilibrium contact angles follow the order smooth biodiesel combustion-particle surface < rough biodiesel combustion-particle surface < rough diesel combustion-particle surface. The corresponding values are 45.4°, 63.5°, and 95.5°, respectively. Wettability increases as θ_{eq} decreases. At fixed surface chemistry, increasing roughness raises

θ_{eq} by approximately 18.1°. At fixed roughness, the lower abundance of polar surface sites further raises θ_{eq} by approximately 32.0°. These results show that both surface microtopography and chemical composition strongly influence particle wettability.

To further interpret changes in the equilibrium contact angle from an energetic perspective, the work of adhesion at the solid-liquid interface was used to quantify interfacial binding strength. The work of adhesion was evaluated using both direct integration and Young–Dupré back-calculation. In the direct-integration approach, the solid-liquid interaction energy E_{int} was obtained from the total potential energy, the particle-substrate potential energy, and the water-phase potential energy. The work of adhesion W_{adh} was then calculated by normalizing E_{int} by the contact area between the droplet and the substrate:

$$E_{int} = E_{tot} - E_{sub} - E_{water} \tag{6}$$

$$W_{adh} = -\frac{E_{int}}{A_c} \tag{7}$$

where E_{tot} is the total potential energy of the system, E_{sub} is the potential energy of the particle substrate, E_{water} is the potential energy of the water phase, and A_c is the equivalent solid-liquid contact area.

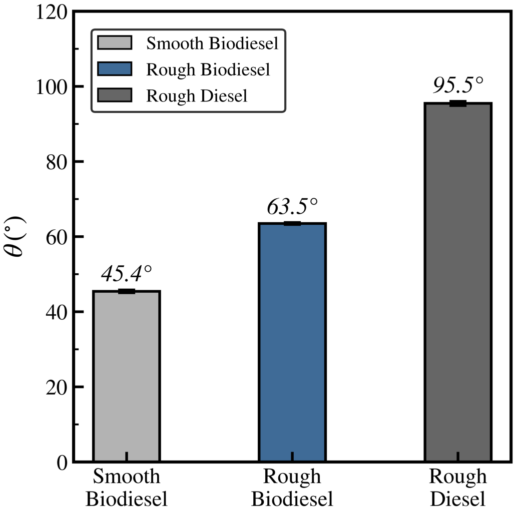

Figure 5: Equilibrium contact angles under different roughness levels and fuel types.

The equivalent solid-liquid contact area A_c was obtained from the production trajectory. For each frame, the vector from the particle center to the droplet center of mass was defined as the contact axis, and water oxygen atoms within 3.5 Å of the particle surface were assigned to the contact layer. The 95th percentile of the polar-angle distribution of these atoms relative to the contact axis was taken as the contact half-angle α_c. A_c was then calculated from the spherical-cap area. The frame-averaged A_c over the sampling window was used to normalize W_{adh}. The per-frame contact area was calculated as:

$$A = 2\pi R^2(1 - \cos\alpha_c) \tag{8}$$

where R is the particle radius and α_c is the contact half-angle.

The Young–Dupré method calculates the work of adhesion W_{adh} from the equilibrium contact angle and the liquid-vapor interfacial tension, thereby providing an energetically based cross-check of the direct-integration results [32]:

$$W_{adh} = \gamma_{LV}\left(1+\cos\theta_{eq}\right) \tag{9}$$

where γ_{LV} is the liquid-vapor interfacial tension and θ_{eq} is the equilibrium contact angle.

Fig. 6 compares the work of adhesion obtained by the two methods. Biodiesel combustion particles exhibit substantially higher work of adhesion than diesel combustion particles. According to the Young–Dupré method, the values are 77 and 48 $\mathrm{mJ\cdot m^{-2}}$, respectively; according to the direct-integration method, they are 60 and 31 $\mathrm{mJ\cdot m^{-2}}$. Although the absolute values differ because the two methods rely on different physical definitions and length-scale assumptions, the trends are consistent, indicating stronger interfacial binding between biodiesel combustion particles and water droplets. Taken together with Figs. 5 and 6, these results show that, at fixed chemical composition, surface roughness increases the contact angle and reduces interfacial binding strength, thereby suppressing droplet spreading by restricting contact-line advance. This interpretation is consistent with current understanding of contact-line pinning and contact-angle hysteresis on rough or chemically heterogeneous surfaces [13–16,27]. Biodiesel combustion particles more readily form stable interactions with water molecules and therefore exhibit stronger wettability than diesel combustion particles.

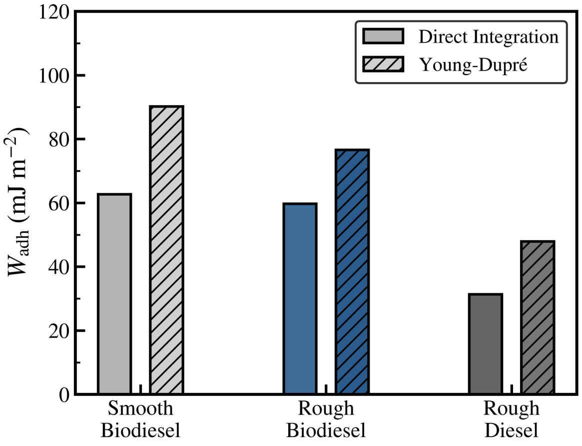

Figure 6: Comparison of the work of adhesion for biodiesel and diesel combustion particles.

3.2 Competitive Processes at the Solid-Liquid Interface

Fig. 7 shows how the equilibrium contact angle of biodiesel combustion particles varies with temperature and saturation ratio. At saturation ratios of 0.8 and 1.0, θ_{eq} decreases slightly over 300–333 K and increases markedly over 333–360 K. At a saturation ratio of 1.0, θ_{eq} values at 300, 333, and 360 K are 51.8°, 45.2°, and 63.1°, respectively, indicating nonmonotonic temperature dependence. At a saturation ratio of 1.2, the corresponding values are 64.4°, 63.5°, and 59.1°, respectively, indicating only a weak temperature dependence. Over 300–333 K, θ_{eq} increases with saturation ratio, whereas at 360 K it first increases and then decreases with increasing saturation ratio. These results show that temperature and saturation ratio have coupled effects on the final wetting state.

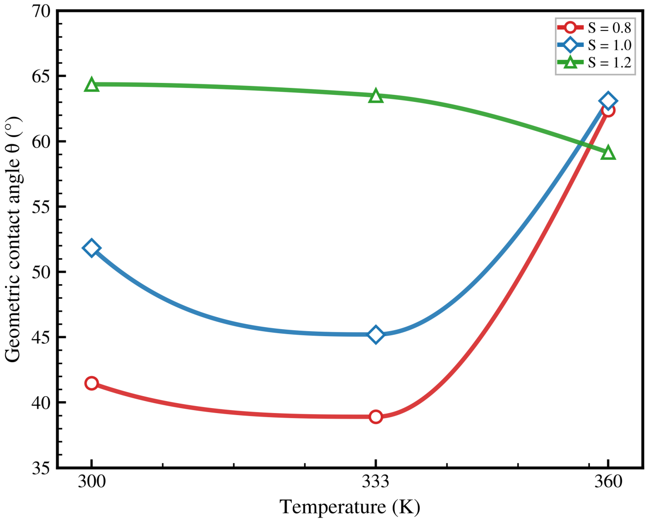

Figure 7: Effects of temperature and saturation ratio on the equilibrium contact angle.

To interpret this behavior, the competition between vapor-phase supply and liquid-phase rearrangement was analyzed from the perspective of molecular exchange at the solid-liquid interface. The rate J_{supply} of outer-layer water entering the droplet was used to characterize vapor-phase supply, the rearrangement rate J_{rearr} of droplet water molecules toward the contact-line vicinity was used to characterize liquid-phase rearrangement, and *RSR* was used to quantify the relative dominance of J_{supply} and J_{rearr}. These metrics were calculated as follows:

$$J_{supply} = (N_{V\to B} + N_{V\to C})/\Delta t \tag{10}$$

$$J_{rearr} = N_{B\to C}/\Delta t \tag{11}$$

$$RSR = \langle J_{supply} \rangle / \langle J_{rearr} \rangle \tag{12}$$

where N is the number of molecules, and the subscripts B, C, and V denote the droplet bulk region, the contact-line vicinity, and the outer-layer water region, respectively.

During interfacial data analysis, the primary droplet was identified from water-molecule clustering and the density field. The droplet bulk region B, contact-line vicinity C, and outer-layer water region V were then defined, and transfer rates from V to B or C and from B to C were counted. Fig. 8 shows that *RSR* is strongly temperature dependent. At 300 K, *RSR* is 0.94–1.10 across saturation ratios, indicating comparable outer-layer supply and liquid-phase rearrangement. At 333 K, *RSR* increases to 1.12–1.59, suggesting a relative strengthening of outer-layer water supply. At 360 K, *RSR* further increases to 3.72–5.42, showing that vapor-phase supply becomes dominant. To further analyze this change, the hydrogen bond density at the solid-water interface of each case was statistically calculated, and the results are shown in Table 4. At 300 and 333 K, the interfacial hydrogen-bond density decreases as the saturation ratio increases, indicating that additional outer-layer water is not necessarily converted into stable bonding in the contact layer. At 360 K, the interfacial hydrogen-bond density narrows to 0.072–0.074 nm^{-2} and θ_{eq} to 59.15°–63.11°, suggesting that enhanced vapor-phase supply and liquid-phase exchange are partly offset by stronger thermal disorder at the interface. Therefore, a higher saturation ratio promotes spreading only when added water contributes to contact-line rearrangement and stable solid-liquid bonding.

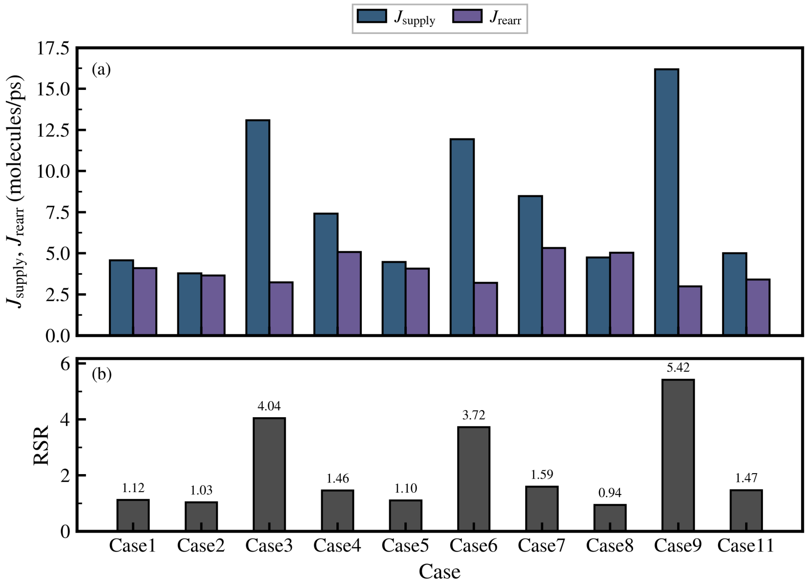

Figure 8: Quasi-steady interfacial exchange competition metrics for cases 1–9 and 11. (**a**) The rate of outer-layer water entering and water molecules rearrangement. (**b**) The ratio of J_{supply} and J_{rearr}.

Table 4: Equilibrium contact angle and interfacial hydrogen-bond density for rough-surface cases.

Case	Type/Surface	T (K)	S	θ_{eq} (°)	Interfacial H-Bond Density (nm^{-2})
Case 1	Biodiesel/rough	333	1.2	63.51	0.076
Case 2	Biodiesel/rough	300	1.2	64.36	0.099
Case 3	Biodiesel/rough	360	1.2	59.15	0.073
Case 4	Biodiesel/rough	333	1.0	45.20	0.150
Case 5	Biodiesel/rough	300	1.0	51.83	0.142
Case 6	Biodiesel/rough	360	1.0	63.11	0.074
Case 7	Biodiesel/rough	333	0.8	38.90	0.180
Case 8	Biodiesel/rough	300	0.8	41.47	0.218
Case 9	Biodiesel/rough	360	0.8	62.38	0.072
Case 11	Diesel/rough	333	1.2	95.47	0.039

These results indicate that the wettability of biodiesel combustion particles is governed by the coupled effects of vapor-phase water supply, solid-liquid interfacial exchange, interfacial bonding, and contact-line motion. Temperature mainly affects interfacial molecular exchange and liquid-phase rearrangement, whereas the saturation ratio further regulates outer-layer water supply and its conversion into rearrangement near the contact line and stable solid-liquid bonding. Together, these processes determine the stability of interfacial bonding and the final wetting state, consistent with the experimental observations of Northrop et al. [20].

3.3 Effects of Functional Groups on Wettability

The surface chemical composition of particles also influences water-droplet spreading. To examine the role of oxygen-containing functional groups in interfacial hydration, the radial distribution function g(r) was used to characterize the local distribution of water molecules near different oxygen sites. Characteristic atoms in surface functional groups were used as reference centers, and g(r) was defined as the ratio of the local number density of water molecules at a distance r to the average number density in the droplet bulk region. The first peak of g(r) reflects the preferred separation distance between water molecules and functional groups, whereas the peak intensity and width reflect the strength and spatial extent of local hydration. As shown in Fig. 9, oxygen-containing sites on both biodiesel and diesel combustion particles exhibit first peaks within r ≈ 2.9–3.4 Å, indicating that polar oxygen sites in both systems can induce local hydration structures. The main difference lies in peak intensity and enriched-site coverage: multiple oxygen-containing sites on biodiesel particles show pronounced water enrichment, whereas diesel particles exhibit high peaks only near a limited number of sites. This indicates that the higher O/C ratio and richer oxygen-containing sites of biodiesel particles help expand the interfacial hydration region. By contrast, hydration on diesel particles is more localized, and the spatial coverage and continuity of the interfacial hydration layer are relatively limited. Therefore, the spatial distribution of interfacial water molecules depends not only on the total abundance of oxygen-containing sites but also on functional-group type and local chemical environment.

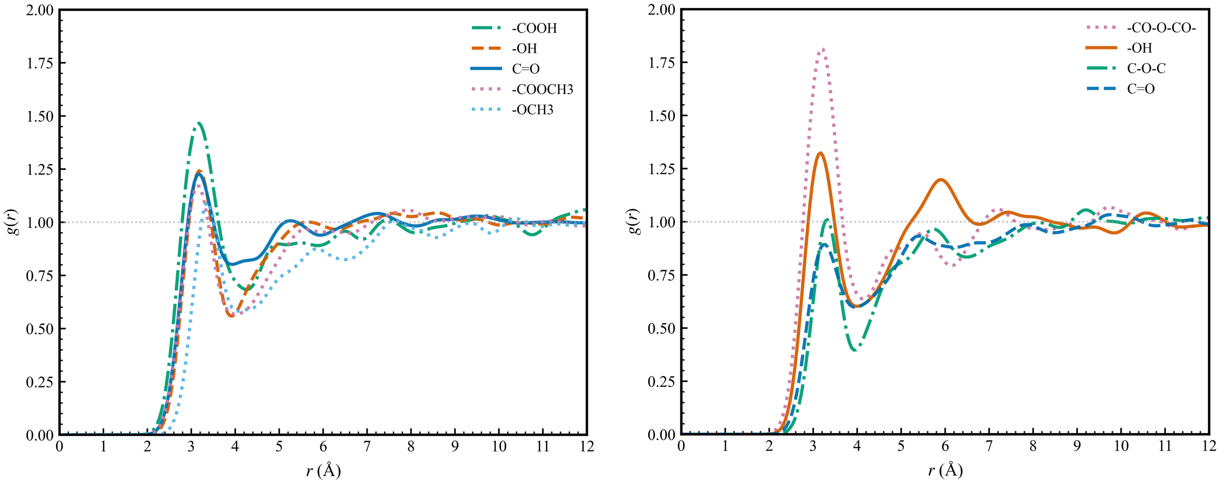

(**a**) (**b**)

Figure 9: Radial distribution functions between surface functional groups and water molecules on combustion particles. (**a**) RDFs of biodiesel combustion particles; (**b**) RDFs of diesel combustion particles.

The RDF mainly reflects the local spatial distribution of water molecules and cannot directly characterize the number and persistence of interfacial bonds. Therefore, solid-liquid interfacial hydrogen bonds were further counted, and their stability was evaluated using the continuous hydrogen-bond autocorrelation function. At 333 K and a saturation ratio of 1.2, rough biodiesel combustion particles have 65.19 ± 5.98 interfacial hydrogen bonds on average, substantially more than the corresponding 27.58 ± 4.02 on rough diesel combustion particles. Water-donor hydrogen bonds dominate in both systems, with corresponding numbers of 59.14 ± 5.36 and 24.52 ± 3.76, respectively. The 1/e decay times of water-donor hydrogen bonds are 1.13 and 1.10 ps for the two systems, respectively, showing only a small difference. Thus, the stronger wettability of biodiesel particles mainly arises from the increased number of bond-forming sites and the higher density of the interfacial hydrogen-bond network, rather than from a marked extension of individual hydrogen-bond lifetimes.

To quantify differences among oxygen sites, the nonbonded interaction energy between water molecules and oxygen sites in different oxygen-containing functional groups was decomposed (Table 5).

Table 5 shows that C=O oxygen sites provide the dominant attractive contribution on both biodiesel and diesel particle surfaces, while –COOH sites also make a notable attractive contribution on biodiesel particles. In contrast, –OCH$_3$ sites show weak unfavorable contributions, indicating that the presence of oxygen functionality alone does not necessarily strengthen attraction to water; the magnitude and sign of the interaction also depend on functional-group type and local charge distribution. Overall, biodiesel particles contain more strongly polar sites, especially C=O and –COOH, which is consistent with their higher interfacial hydrogen-bond density and smaller equilibrium contact angle. The rough biodiesel surface shows a slightly stronger oxygen-site attraction than the smooth surface, but its apparent equilibrium contact angle is larger, indicating that enhanced local hydration and bonding do not necessarily translate into greater spreading because contact-line pinning and geometric hindrance on nanoscale roughness can limit continuous droplet expansion.

Table 5: Nonbonded interaction energy decomposition between functional-group oxygen sites and water molecules.

Surface	Oxygen Site	N	E/(kcal·mol^{-1})	E/N/(kcal·mol^{-1})	$\lvert E\rvert$ Fraction/%
Smooth biodiesel	C=O oxygen	1116	−703.00	−0.630	65.7
Smooth biodiesel	–COOH oxygen	2366	−167.73	−0.071	15.6
Smooth biodiesel	–COOCH$_3$ oxygen	4604	−55.78	−0.012	5.3
Smooth biodiesel	–OH oxygen	2527	+45.42	+0.018	4.5
Smooth biodiesel	–OCH$_3$ oxygen	1833	+95.04	+0.052	8.9
Rough biodiesel	C=O oxygen	1187	−756.93	−0.638	63.6
Rough biodiesel	–COOH oxygen	2340	−223.91	−0.096	18.7
Rough biodiesel	–COOCH$_3$ oxygen	4552	−64.75	−0.014	5.4
Rough biodiesel	–OH oxygen	2537	−45.49	−0.018	4.0
Rough biodiesel	–OCH$_3$ oxygen	1843	+98.47	+0.053	8.3
Rough diesel	C=O oxygen	1014	−211.16	−0.208	42.2
Rough diesel	–CO–O–CO– oxygen	1890	−191.59	−0.101	38.0
Rough diesel	C–O–C oxygen	2703	−63.26	−0.023	12.6
Rough diesel	–OH oxygen	1389	−37.48	−0.027	7.3

Note: E is the nonbonded interaction energy between oxygen sites and water molecules, and N is the number of oxygen sites. Negative and positive values indicate attractive and unfavorable contributions, respectively. The $\lvert E\rvert$ fraction compares the relative interaction strength of different oxygen sites on the same surface.

Taken together, the RDF, hydrogen-bond statistics, and oxygen-site energy decomposition show that the stronger wettability of biodiesel combustion particles relative to diesel combustion particles mainly arises from richer polar oxygen-containing sites, a higher number of interfacial bonds, and a more continuous local hydration structure. The comparison of interfacial density and pressure distributions in Fig. 10 further supports this interpretation: the high-density water layer on biodiesel combustion particles lies closer to the solid surface and exhibits more pronounced lateral spreading, whereas the interfacial water layer on diesel combustion particles is more diffuse and has a broader pressure-perturbation range. These results show that oxygen-containing functional groups increase the wetting tendency of particles by promoting local hydration and interfacial bonding. For rough surfaces, however, enhanced local hydration and bonding do not necessarily translate fully into macroscopic spreading, because contact-line pinning and geometric hindrance may still restrict droplet expansion.

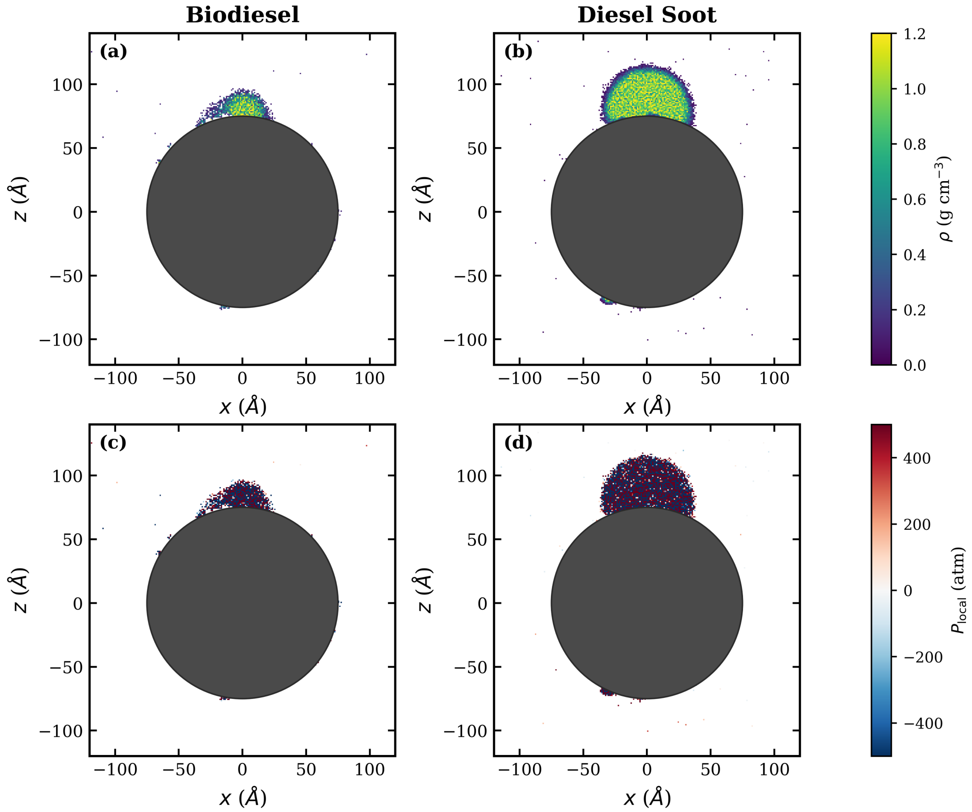

Figure 10: Comparison of interfacial structures and mechanical fields between biodiesel and diesel combustion particles. (**a**) Interfacial water density distribution for biodiesel particles. (**b**) Interfacial water density distribution for diesel particles. (**c**) Interfacial pressure distribution for biodiesel particles. (**d**) Interfacial pressure distribution for diesel particles.

4 Conclusions

Using molecular dynamics simulations based on a unified defective carbon framework, this study systematically investigated the wetting behavior of biodiesel and diesel combustion particles under representative plume-region temperature and saturation-ratio conditions. The microscopic mechanisms were analyzed in terms of contact angle, work of adhesion, interfacial exchange, hydrogen-bond networks, and functional-group site interactions. The main conclusions are as follows:

1. Surface roughness suppresses continuous droplet spreading and increases the apparent equilibrium contact angle. At 333 K and a saturation ratio of 1.2, the equilibrium contact angles of smooth biodiesel, rough biodiesel, and rough diesel combustion particles are 45.4°, 63.5°, and 95.5°, respectively. Compared with diesel combustion particles, biodiesel combustion particles exhibit a smaller contact angle and a larger work of adhesion.
2. Particle wetting behavior is governed by the competition among vapor-phase water supply, liquid-phase rearrangement, interfacial bonding, and contact-line motion. As temperature increases from 300 to 360 K, RSR increases from 0.94–1.10 to 3.72–5.42, indicating stronger outer-layer water supply relative to contact-line rearrangement. Saturation ratio regulates spreading by modulating the contribution of added water to stable solid-liquid bonding and contact-line motion.
3. The stronger wettability of biodiesel combustion particles mainly originates from richer polar oxygen-containing sites, more interfacial hydrogen bonds, and a more continuous hydration structure.

Hydrogen-bond lifetime analysis and oxygen-site energy decomposition indicate that this enhancement mainly arises from solid-liquid attraction provided by C=O and –COOH sites and from the increased number of interfacial bonds.

Acknowledgement: Not applicable.

Funding Statement: This work was supported by the National Natural Science Foundation of China (No. 51876133).

Author Contributions: Yifan Liu: investigation, data curation, visualization, writing—original draft. Dengpan Zhang: conceptualization, investigation, validation, writing—review & editing. Jiayi Du: methodology, validation. Deqing Mei: conceptualization, formal analysis. Yinnan Yuan: supervision, funding acquisition. All authors reviewed and approved the final version of the manuscript.

Availability of Data and Materials: The datasets and model files generated and/or analyzed during the current study are available from the corresponding author upon reasonable request.

Ethics Approval: Not applicable. This study did not involve human participants, human data, or animals.

Conflicts of Interest: The authors declare no conflicts of interest.

References

1. Pope IIICA, Dockery DW. Health effects of fine particulate air pollution: lines that connect. J Air Waste Manag Assoc. 2006;56(6):709–42. doi:10.1080/10473289.2006.10464485.
2. Vogt R, Scheer V, Casati R, Benter T. On-road measurement of particle emission in the exhaust plume of a diesel passenger car. Environ Sci Technol. 2003;37(18):4070–6. doi:10.1021/es0300315.
3. Lipsky EM, Robinson AL. Effects of dilution on fine particle mass and partitioning of semivolatile organics in diesel exhaust and wood smoke. Environ Sci Technol. 2006;40(1):155–62. doi:10.1021/es050319p.
4. Weingartner E, Burtscher H, Baltensperger U. Hygroscopic properties of carbon and diesel soot particles. Atmos Environ. 1997;31(15):2311–27. doi:10.1016/S1352-2310(97)00023-X.
5. Deshmukh S, Poulain L, Wehner B, Henning S, Petit JE, Fombelle P, et al. External particle mixing influences hygroscopicity in a sub-urban area. Atmos Chem Phys. 2025;25(2):741–58. doi:10.5194/acp-25-741-2025.
6. Zeng L, Hu S, Fang W, Chen Z, Xie Y, Chen S, et al. Insights into the evolution behavior and hygroscopicity of black carbon-containing particles based on observations of their chemical compositions in Beijing's autumn. J Geophys Res Atmos. 2025;130(12):e2024JD043180. doi:10.1029/2024jd043180.
7. Vehkamäki H, Kulmala M, Lehtinen KEJ, Noppel M. Modelling binary homogeneous nucleation of water-sulfuric acid vapours: parameterisation for high temperature emissions. Environ Sci Technol. 2003;37(15):3392–8. doi:10.1021/es0263442.
8. Petters MD, Kreidenweis SM. A single parameter representation of hygroscopic growth and cloud condensation nucleus activity. Atmos Chem Phys. 2007;7(8):1961–71. doi:10.5194/acp-7-1961-2007.
9. Taherian F, Marcon V, van der Vegt NFA, Leroy F. What is the contact angle of water on graphene? Langmuir. 2013;29(5):1457–65. doi:10.1021/la304645w.
10. Werder T, Walther JH, Jaffe RL, Halicioglu T, Koumoutsakos P. On the water–carbon interaction for use in molecular dynamics simulations of graphite and carbon nanotubes. J Phys Chem B. 2003;107(6):1345–52. doi:10.1021/jp0268112.
11. Guissani Y, Guillot B. A computer simulation study of the liquid-vapor coexistence curve of water. J Chem Phys. 1993;98(10):8221–35. doi:10.1063/1.464527.
12. Jiang H, Müller-Plathe F, Panagiotopoulos AZ. Contact angles from Young's equation in molecular dynamics simulations. J Chem Phys. 2017;147(8):084708. doi:10.1063/1.4994088.
13. Law KY. Contact angle hysteresis on smooth/flat and rough surfaces. Interpretation, mechanism, and origin. Acc Mater Res. 2022;3(1):1–7. doi:10.1021/accountsmr.1c00051.

14. Koishi T, Yasuoka K, Fujikawa S, Zeng XC. Measurement of contact-angle hysteresis for droplets on nanopillared surface and in the Cassie and Wenzel states: a molecular dynamics simulation study. ACS Nano. 2011;5(9):6834–42. doi:10.1021/nn2005393.
15. Ramiasa M, Ralston J, Fetzer R, Sedev R, Fopp-Spori DM, Morhard C, et al. Contact line motion on nanorough surfaces: a thermally activated process. J Am Chem Soc. 2013;135(19):7159–71. doi:10.1021/ja3104846.
16. Tsao YH, Wang TY, Tsao HK, Sheng YJ. Thermally assisted mobility of nanodroplets on surfaces with weak defects. J Colloid Interface Sci. 2021;604(2):150–6. doi:10.1016/j.jcis.2021.06.163.
17. Liu J, Zhang X, Tang C, Wang L, Sun P, Wang P. Effects of palm oil biodiesel addition on exhaust emissions and particle physicochemical characteristics of a common-rail diesel engine. Fuel Process Technol. 2023;241(8):107606. doi:10.1016/j.fuproc.2022.107606.
18. Wei J, Wang Y. Effects of biodiesels on the physicochemical properties and oxidative reactivity of diesel particulates: a review. Sci Total Environ. 2021;788:147753. doi:10.1016/j.scitotenv.2021.147753.
19. Du JY, Jiang S, Zhang DP, Yang QH, Pang DQ, Yuan YN. Study on oxygen-containing functional group and oxidation activity on the surface of biodiesel particles. Trans CSICE. 2021;39(5):395–401. (In Chinese). doi:10.16236/j.cnki.nrjxb.202105050.
20. Northrop WF, Madathil PV, Bohac SV, Assanis DN. Condensational growth of particulate matter from partially premixed low temperature combustion of biodiesel in a compression ignition engine. Aerosol Sci Technol. 2011;45(1):26–36. doi:10.1080/02786826.2010.517579.
21. Han S, Hong J, Luo Q, Xu H, Tan H, Wang Q, et al. Hygroscopicity of organic compounds as a function of organic functionality, water solubility, molecular weight, and oxidation level. Atmos Chem Phys. 2022;22(6):3985–4004. doi:10.5194/acp-22-3985-2022.
22. Du J, Qin J, Zhang D, Jiang S, Yuan Y. Effects of surface functional groups on the wettability of biodiesel combustion particulate matter. J Energy Inst. 2024;114(10):101604. doi:10.1016/j.joei.2024.101604.
23. Hu Z, Fu J, Gao X, Lin P, Zhang Y, Tan P, et al. Waste cooking oil biodiesel and petroleum diesel soot from diesel bus: a comparison of morphology, nanostructure, functional group composition and oxidation reactivity. Fuel. 2022;321(2):124019. doi:10.1016/j.fuel.2022.124019.
24. Ishiguro T, Takatori Y, Akihama K. Microstructure of diesel soot particles probed by electron microscopy: first observation of inner core and outer shell. Combust Flame. 1997;108(1–2):231–4. doi:10.1016/S0010-2180(96)00206-4.
25. Maple JR, Hwang MJ, Stockfisch TP, Dinur U, Waldman M, Ewig CS, et al. Derivation of class II force fields. I. Methodology and quantum force field for the alkyl functional group and alkane molecules. J Comput Chem. 1994;15(2):162–82. doi:10.1002/jcc.540150207.
26. Berendsen HJC, Grigera JR, Straatsma TP. The missing term in effective pair potentials. J Phys Chem. 1987;91(24):6269–71. doi:10.1021/j100308a038.
27. Giacomello A, Schimmele L, Dietrich S. Wetting hysteresis induced by nanodefects. Proc Natl Acad Sci U S A. 2016;113(3):E262–71. doi:10.1073/pnas.1513942113.
28. Santiso E, Herdes C, Müller E. On the calculation of solid-fluid contact angles from molecular dynamics. Entropy. 2013;15(9):3734–45. doi:10.3390/e15093734.
29. Smith ER, Müller EA, Craster RV, Matar OK. A Langevin model for fluctuating contact angle behaviour parametrised using molecular dynamics. Soft Matter. 2016;12(48):9604–15. doi:10.1039/c6sm01980c.
30. Irving JH, Kirkwood JG. The statistical mechanical theory of transport processes. IV. The equations of hydrodynamics. J Chem Phys. 1950;18(6):817–29. doi:10.1063/1.1747782.
31. Vega C, de Miguel E. Surface tension of the most popular models of water by using the test-area simulation method. J Chem Phys. 2007;126(15):154707. doi:10.1063/1.2715577.
32. Good RJ. Contact angle, wetting, and adhesion: a critical review. J Adhes Sci Technol. 1992;6(12):1269–302. doi:10.1163/156856192X00629.